

Enhanced Fault-tolerance in Photonic Quantum Computing: Floquet Code Outperforms Surface Code in Tailored Architecture

Paul Hilaire,^{1,*} Théo Dessertaine,¹ Boris Bourdoncle,¹ Aurélie Denys,¹
Grégoire de Gliniasty,^{1,2} Gerard Valentí-Rojas,^{3,4} and Shane Mansfield¹

¹*Quandela, 7 Rue Léonard de Vinci, 91300 Massy, France*

²*Sorbonne Université, CNRS, LIP6, F-75005 Paris, France*

³*Naquidis Center, Institut d'Optique Graduate School, 91127, Palaiseau, France*

⁴*Institut de Mathématiques de Bordeaux, UMR 5251, Université de Bordeaux, France*

(Dated: 10th October 2024)

Fault-tolerant quantum computing is crucial for realizing large-scale quantum computation, and the interplay between hardware architecture and quantum error-correcting codes is a key consideration. We present a comparative study of two quantum error-correcting codes – the surface code and the honeycomb Floquet code – implemented on variants of the spin-optical quantum computing architecture, enabling a direct comparison of the codes using consistent noise models. Our results demonstrate that the honeycomb Floquet code significantly outperforms the surface code in this setting. Notably, we achieve a photon loss threshold of 6.4% for the honeycomb Floquet code implementation – to our knowledge the highest reported for photonic platforms to date without large-scale multiplexing. This finding is particularly significant given that photon loss is the primary source of errors in photon-mediated quantum computing.

Introduction. Fault-tolerant quantum computing aims at reliable information processing even in the presence of physical noise, which in theory is made possible by the threshold theorem [1]. Fault-tolerance via quantum error correction is necessary to achieve large-scale quantum computation capable of implementing the kinds of high-impact applications that would derive for instance from Shor’s factoring algorithm [2], or the Harrow-Hassidim-Lloyd algorithm [3] for solving linear systems.

In the pursuit of practical fault-tolerant quantum computing, the interplay between hardware architecture and quantum error-correcting codes is a crucial consideration. In this article we evidence the point with a comparative performance of two kinds of code – the surface code [4] and the honeycomb Floquet code [5] – when implemented with two variants of the spin-optical quantum computing (SPOQC) architecture [6].

This modular architecture has been designed specifically for computing platforms consisting of quantum dot photon emitters [7–12], photon routers and small linear optical circuits. These same basic modules have already been used to realise small-scale noisy quantum computing platforms [13]. However, the architecture may equally be realized using other kinds of photon emitters that have an embedded qubit degree of freedom (e.g. [14–16]).

In the original version of the SPOQC architecture linear optical circuits were used to perform “repeat-until-success” (RUS) controlled-Z gates. These are especially convenient for running error correction, for example via the popular surface code (SC) [4]. The SC allows fault-tolerance [17] and is attractive for its versatility and simplicity, admitting a 2D planar layout and good error thresholds. In particular it has recently been implemented at small scale below threshold on real hard-

ware [18]. Combined with the SPOQC architecture the SC was shown to allow a photon loss threshold of 2.8% [6].

However, a limitation of the SC is that it relies on the measurement of weight-4 Pauli operators to check for errors, and high-weight measurements are challenging to implement in practice. A typical way to circumvent this is by using syndrome extraction circuits, in which four two-qubit entangling gates and an ancilla qubit allow for indirect measurement of the check operator [19].

In this context, the recent development of a new family of codes known as Floquet codes [20–26] opens exciting new possibilities. Through periodic sequences of weight-2 measurements, such codes dynamically generate effective stabilizers of higher weight over time. In this way they can achieve the benefits of higher-weight check operators, while only requiring simpler lower-weight measurements. This makes them well-suited to technological platforms for which such operations are native, i.e. easy to implement, such as photonic platforms [27] or Majorana-based qubits [28]. Of particular interest is the honeycomb Floquet code (HC) [5], which may be understood as a dynamical version, or “floquetification” of the SC, in the sense that it switches between three implementations of the SC.

An existing comparison indicates that the HC performs significantly better than the SC on hardware with native two-qubit measurements [29]. However, the comparison relied on different noise models for the native operations used to implement the respective codes.

We establish conclusively that the SC is outperformed by its “floquetified” version, the HC, when implemented with appropriate variants of the SPOQC architecture – specifically with controlled-Z gates for the SC and with RUS ZZ measurements for the HC. Crucially, the same noise model applies to both two-qubit gates and two-

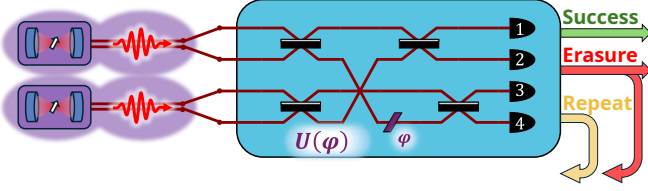


Figure 1: Sketch of a RUS operation using a linear-optical interferometer $U(\varphi)$. The nature of the operation depends on the phase φ : if $\varphi = \pi/2$, the target operation is a CZ between the spins; if $\varphi = 0$, it's an M_{ZZ} measurement of the spins. Both operations can be repeated, but the attempted CZ must be abandoned when an erasure outcome is obtained, while the attempted M_{ZZ} can still succeed despite the erasure. The M_{ZZ} operation can thus be repeated until success even in that case.

qubit measurements.

Remarkably, we obtain a photon loss threshold of 6.4%, which to our knowledge is the best that has been reported to date for photonic platforms [6, 27] that do not rely on large-scale multiplexing [30–36]. This is all the more important given that photon loss is the primary source of errors in photon-mediated quantum computing platforms.

Repeat-until-success operations. Linear-optical repeat-until-success (RUS) controlled-Z gates, CZ, and two-qubit ZZ measurements, M_{ZZ} , acting on spin qubits are native operations for spin-optical platforms. Embedded in a fault-tolerant architecture, they provide an interesting performance test bed for numerical simulations since they have precisely the same error model despite performing very different operations: an entangling gate and a non-destructive measurement respectively. The RUS operation [37] relies on a probabilistic linear-optical subroutine which is repeated until the desired outcome is obtained. The subroutine, illustrated in Figure 1, is as follows.

1. Each quantum emitter generates a spin-entangled photon through the process E [7–12, 15, 16]:

$$E = |0_s, 0_{ph}\rangle \langle 0_s| + |1_s, 1_{ph}\rangle \langle 1_s|, \quad (1)$$

where the subscripts “s” and “ph” respectively denote the spin qubit and dual-rail-encoded photonic qubit [38].

2. The two spin-entangled photons enter a 4-mode linear-optical interferometer that performs a unitary transformation $U(\varphi)$ on its input optical modes.
3. The photons are detected by photon-number-resolving detectors located at the end of each linear-optical interferometer output modes.

The classical signal describing where photons were detected is a measurement pattern. The measurement patterns for which two photons are detected can be divided

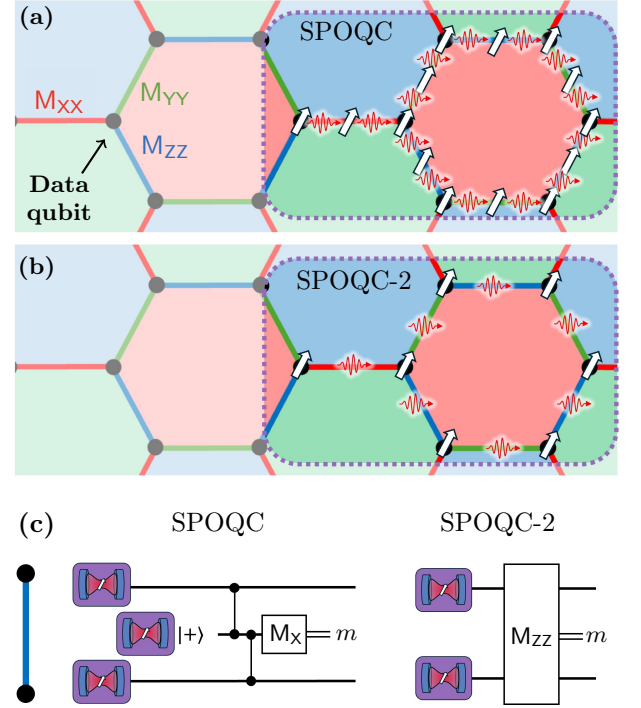


Figure 2: Honeycomb Floquet code defined by a sequence of M_{XX} , M_{YY} and M_{ZZ} measurements on red, green and blue edges of a tri-colorable hexagonal lattice, with architecture layout for the (a) SPOQC and (b) SPOQC-2 architectures. The white arrows represent quantum emitters and the undulating red arrows represent linear-optical RUS operations. (c) Implementation of an M_{ZZ} measurement for the SPOQC (left) and SPOQC-2 (right) architectures, where m denotes the measurement result.

into two categories. **Success** patterns correspond to successfully performing the desired operation on the spins, up to local rotations, while **repeat** patterns correspond to performing the identity gate on the spins, up to local rotations. In the ideal case, the subroutine is repeated until a success pattern is obtained. The operation that we perform, either a CZ gate or an M_{ZZ} measurement, depends on the phase φ of a single phase-shifter of the interferometer. Setting $\varphi = \pi/2$ performs a spin CZ gate, and $\varphi = 0$ performs an M_{ZZ} measurement.

In the presence of photon loss, there is a non-zero probability that fewer than two photons are detected, leading to **erasure** outcomes. In that case, we obtain a heralded error that corresponds to two phase erasures

$$\mathcal{C}_{\text{RUS},f}(\rho) = \mathcal{C}_a \circ \mathcal{C}_b(\rho), \quad (2)$$

where a, b denote the spin qubits and $\mathcal{C}_i(\rho) = (\rho + Z_i \rho Z_i)/2$. We assume that each photon has the same loss rate ε . The **erasure** outcome then has a probability $p_e = 1 - (1 - \varepsilon)^2$ while the **repeat** and **success** outcomes both have a probability $p_r = p_s = (1 - \varepsilon)^2/2$.

For simplicity, we assume the subroutine is repeated as many times as necessary to obtain a success or failure event, i.e., the maximum number of RUS trials is unbounded. In that case, the overall RUS failure probability is

$$p_{\text{RUS}} = \frac{2 - 2(1 - \varepsilon)^2}{2 - (1 - \varepsilon)^2}, \quad (3)$$

as derived in [38]. In practice, the protocol terminates after an average number $(p_s + p_e)^{-1}$ of trials for RUS CZ (p_s^{-1} for RUS M_{ZZ}).

Crucially, the error channel in Eq. (2) and its heralding probability p_{RUS} are the same for both a CZ gate and an M_{ZZ} measurement. Moreover, photon distinguishability and spin decoherence errors [38], two other typical errors for these platforms, also act in the same way for both operations. This puts the operations on an equal footing, enabling a fair comparison between architectures relying natively on one or the other. More details on the RUS operations can be found in [6, 37].

Spin-optical architectures and the honeycomb Floquet code. Our SPOQC architecture variants rely on either native CZ gates or M_{ZZ} measurements. Although they are compatible with arbitrary quantum error-correcting codes, our focus here is on the planar HC code [39]. In this dynamical code, data qubits are located on the vertices of a planar hexagonal tiling. The edges correspond to two-qubit non-destructive measurements on the incident data qubits. Such a tiling is edge tri-colorable and we associate to each edge a color: red, green, and blue edges will correspond to M_{XX}, M_{YY}, and M_{ZZ} measurements, respectively; i.e. an AA measurement, where A is a Pauli X, Y, or Z operator. At a given time step we measure all the edges of a given color in the corresponding measurement basis. We repeatedly perform the measurement sequence “red-green-blue-red-blue-green” which is compatible with the planar layout [40] of Figure 2(a).

The original SPOQC architecture [6] implements the code with RUS CZ gates. In this architecture, physical qubits are spin qubits embedded in quantum emitters. We perform the syndrome extraction – i.e. the detection of errors – through short-depth quantum circuits: additional ancilla qubits are entangled with data qubits using RUS CZ gates to measure check operators. Therefore for the HC, we need spin qubits at each vertex of the hexagonal tiling but also an ancilla qubit and two RUS CZ gates for each edge in Figure 2(a) to perform the two-qubit measurement using the syndrome extraction circuit shown on the left in Figure 2(c).

The architecture variant that we denote SPOQC-2, is a version of SPOQC that exploits native RUS M_{ZZ} measurements. Using spin Hadamard gates $H = H_{XZ} = (X + Z)/\sqrt{2}$ or $H_{YZ} = (Y + Z)/\sqrt{2}$ gates, we can convert M_{ZZ} into M_{XX} or M_{YY} measurements, thus obtaining all measurements necessary to perform the measurement sequence of the HC (see [38] and Figure 2(c) Right). This

Code	Native operation	p_{RUS}	ε	D	t_{RUS}/T_2
Surface code	CZ	10%	2.8%	2.2%	2.3%
	M _{ZZ}	16%	4.3%	1.8%	1.2%
Honeycomb	CZ	6%	1.6%	0.8%	0.6%
Floquet code	M _{ZZ}	22%	6.4%	2.3%	2.3%

Table I: Summary of the achievable individual thresholds rounded to the second significant figure for the surface and honeycomb Floquet codes and for the SPOQC (native CZ operation) and SPOQC-2 (native M_{ZZ} operation) architectures. The largest achievable thresholds for each error are highlighted. SC with CZ results comes from Ref. [6], SC with M_{ZZ} exploits the syndrome extraction circuit from Ref. [43], and HC with both CZ and M_{ZZ} native operations were implemented using the strategy described above.

drastically reduces the numbers of spins and RUS modules required to implement the HC, since we only need one spin qubit per node and one RUS module per edge. This corresponds to halving the number of RUS modules and up to a 60% reduction of the number of spin qubits in the limit of large lattices [41].

The main exploitable difference between RUS CZ gates and RUS M_{ZZ} measurements lies in the way we treat **erasure** outcomes. Since any erasure leads to the complete dephasing of the two spin qubits and the CZ gate acts on the phase. For RUS CZ gates, erasures leads to gate failure. On the other hand, the **erasure** channel commutes with the M_{ZZ} and hence does not change the measurement result. With RUS M_{ZZ} measurements, we thus repeat the subroutine whenever we have an **erasure** outcome. Importantly, this means that we can always recover the measurement outcome by using sufficiently many trials. In other words the success probability of obtaining a meaningful measurement outcome is unity (provided no other errors are considered), compared to the $(1 - p_{\text{RUS}})^2$ probability of the SPOQC architecture, for which two RUS CZ gates need to succeed. We believe this to be the main source of threshold improvement of the SPOQC-2 architecture when tailored to Floquet codes.

However, we also stress that the interest of the SPOQC-2 architecture is not restricted to dynamical codes. We can always design a syndrome extraction circuit based on two-qubit measurements and implement it with the SPOQC-2 architecture [42]. The pentagon tiling of the SC [43] offers a good example of such a design, which we also consider in this article.

Architecture comparison. To compare both architectures, we rely on the computation of *fault-tolerant thresholds*. For a given abstract physical error parameterized by p (typically the physical error probability or a

quantity growing with that probability), the threshold is the value p_{th} under which increasing the size of the code yields increasingly better protection of the logical information. We can thus compare architectures through the various thresholds they offer: the higher these thresholds, the more effective the architecture is at correcting this type of error. In this article, we focus on the threshold specific to an X-type quantum memory, i.e., the preparation and protection of a logical $|+_L\rangle$ state (the Z-type quantum memory actually exhibits consistently similar or larger thresholds). Protecting a quantum memory is the simplest operation required by a fault-tolerant quantum computer, and is therefore an important benchmark for any architecture.

Table I summarises the different threshold values obtained for SPOQC and SPOQC-2 given different photonic error models corresponding to erasures, distinguishability and spin decoherence. Recall that the spin-qubit phase erasures are induced by photon loss. They can thus equivalently be parameterized by the total erasure probability p_{RUS} (Eq. 3) of the RUS gate or by the photon loss rate ε . Distinguishability and decoherence error models are respectively parameterized by $D = 1 - M$ where M is the mean wave-packet overlap between photons, and the ratio t_{RUS}/T_2 between the RUS gate time t_{RUS} and the spin coherence time T_2 . Details on these error mechanisms can be found in the supplementary material [38]. To evaluate the thresholds, we numerically estimate the logical error rates, i.e. the probability of logical information corruption, of HCs of various lattice sizes (parameterized by the distance d of the code) and plot it as a function of the physical error parameter. The crossing point between the curves corresponding to the two largest simulated distances gives an estimation of the fault-tolerant threshold. See [38] for more details. Figure 3 shows the evolution of the logical error rate as a function of p_{RUS} and d , for a HC implemented on the SPOQC-2 architecture. This threshold, or its equivalent for loss, is crucial since photon loss is the most detrimental source of noise in photonic platforms. State-of-the-art photonic experiments still struggle to lower photon loss below about $\varepsilon \approx 30\%$ [44], and it is thus imperative to efficiently correct this error. Here, for the SPOQC-2 architecture with HC, we obtain an erasure threshold of $p_{RUS,th} \approx 21.9\%$, corresponding to a photon loss threshold of $\varepsilon_{th} \approx 6.4\%$.

This is significantly larger than what is achieved with a SC in the SPOQC architecture, for which the threshold is $p_{RUS,th} \approx 10\%$, corresponding to $\varepsilon_{th} \approx 2.8\%$ [6]. Interestingly, the threshold achieved is also superior to the erasure threshold obtained in [27] where a Floquet code was implemented in the fusion-based quantum computing paradigm [30] with linear graph resource states. In that case, the fusion erasure threshold of $\approx 13.2\%$ (related to the p_{RUS} failure) leads to less than $\varepsilon_{th} \leq 1\%$ photon loss threshold [45]. The SC itself can also be

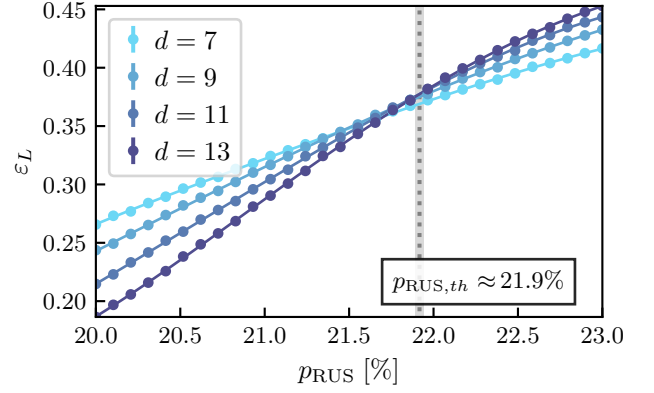


Figure 3: Logical error rate ε_L for different gate failure probability p_{RUS} and HC's distance d within the SPOQC-2 architecture. Error bars on the data points correspond to 99.9% confidence intervals. The dotted gray line marks the approximate threshold value $p_{RUS,th}$. The shaded region encloses values of p_{RUS} within a one-standard-deviation interval around $p_{RUS,th}$.

implemented on the SPOQC-2 architecture since there exist syndrome extraction circuits for the SC that only involve pair measurements [43, 46], for example using a planar pentagon tiling layout. Our simulations show that in that case as well, we reach a larger threshold than with the standard SPOQC architecture, though the threshold obtained is smaller than for the HC.

To fully investigate the performance of both architectures, we also computed thresholds for spin decoherence and photon distinguishability. We found similar thresholds for the HC with SPOQC-2 and the SC with SPOQC, and slightly inferior results for the pair-measurement syndrome extraction circuits of the SC with SPOQC-2. The poorer performances of SC implemented on SPOQC-2 can mostly be explained by the higher depth of the syndrome extraction circuit for the pentagon-tiled SC which allows more time for spin decoherence, as well as the higher number of RUS operations which increases the impact of distinguishability-induced errors.

Discussion. By tailoring the native operations of the spin-optical quantum computing architecture to the honeycomb Floquet code, we observe an improved photon loss threshold of 6.4%, compared to the original 2.8% reported in [6], along with significant reduction in resource overheads. This demonstrates concretely in the case of the SPOQC architecture that it is beneficial to co-design and seek compatibility between quantum error-correcting codes, syndrome extraction methods, and a hardware's native gates. We believe that this observation should also apply to other technological platforms, and we expect that extending the approach to include further building blocks of a fault-tolerant quantum computer, in particu-

lar decoding methods and logical gate implementations, can also prove fruitful, as suggested in [47, 48] in the context of cold atom platforms.

The idea of “floquetifying” quantum error-correcting codes has already been investigated in specific instances (e.g. [20, 24, 49]). Our results lend concrete evidence to these efforts that the use of Floquet codes can lead to significant performance improvements.

Interestingly, we also observe an improvement in the photon loss threshold when implementing the SC with a syndrome extraction circuit exploiting native two-qubit measurements, which suggests that searching for efficient syndrome extraction circuits based on native two-qubit measurements is a noteworthy research avenue. While those available for the SC have recently been improved [50], it would be useful to transpose these results to other codes, such as high-encoding-rate quantum low-density parity-check codes.

Our work not only establishes the superiority of the honeycomb Floquet code over its static counterpart in the appropriate spin-optical quantum computing architecture but also highlights the potential of Floquet codes in advancing fault-tolerant quantum computing on photon-mediated platforms.

Note. While preparing this manuscript, we became aware of a related but independent work on fault-tolerant spin-optical architectures [51] also featuring RUS measurements as well as boosted fusion gates [52].

Acknowledgments. We thank Nicolas Maring, Rawad Mezher, and Noah Shofer for their careful revision of this manuscript. We thank Craig Gidney for the development of the Stim package and for open-sourcing the quantum circuits that we exploit to carry out our simulations. This work has been co-funded by the European Commission as part of the EIC accelerator program under the grant agreement 190188855 for SEPOQC project, by the Horizon-CL4 program under the grant agreement 101135288 for EPIQUE project, and by the CIFRE grant n°2022/0532. G. V-R acknowledges support from the Naquidis Innovation Center for Disruptive Quantum Products.

* paul.hilaire@quandela.com

- [1] D. Aharonov and M. Ben-Or, Fault-tolerant quantum computation with constant error, in *Proceedings of the twenty-ninth annual ACM symposium on Theory of computing* (1997) pp. 176–188.
- [2] P. W. Shor, Algorithms for quantum computation: discrete logarithms and factoring, in *Proceedings 35th annual symposium on foundations of computer science* (Ieee, 1994) pp. 124–134.
- [3] A. W. Harrow, A. Hassidim, and S. Lloyd, Quantum algorithm for linear systems of equations, *Phys. Rev. Lett.* **103**, 150502 (2009).
- [4] S. B. Bravyi and A. Y. Kitaev, Quantum codes on a lattice with boundary, *arXiv preprint quant-ph/9811052* (1998).
- [5] M. B. Hastings and J. Haah, Dynamically Generated Logical Qubits, *Quantum* **5**, 564 (2021).
- [6] G. de Glinasty, P. Hilaire, P.-E. Emeriau, S. C. Wein, A. Salavrakos, and S. Mansfield, A Spin-Optical Quantum Computing Architecture, *Quantum* **8**, 1423 (2024).
- [7] J. P. Lee, B. Villa, A. J. Bennett, R. M. Stevenson, D. J. P. Ellis, I. Farrer, D. A. Ritchie, and A. J. Shields, A quantum dot as a source of time-bin entangled multi-photon states, *Quantum Science and Technology* **4**, 025011 (2019).
- [8] M. H. Appel, A. Tiranov, S. Pabst, M. L. Chan, C. Starup, Y. Wang, L. Midolo, K. Tiurev, S. Scholz, A. D. Wieck, A. Ludwig, A. S. Sørensen, and P. Lodahl, Entangling a hole spin with a time-bin photon: A waveguide approach for quantum dot sources of multiphoton entanglement, *Phys. Rev. Lett.* **128**, 233602 (2022).
- [9] N. Coste, D. Fioretto, N. Belabas, S. Wein, P. Hilaire, R. Frantzeskakis, M. Gundin, B. Goes, N. Somaschi, M. Morassi, *et al.*, High-rate entanglement between a semiconductor spin and indistinguishable photons, *Nature Photonics* **17**, 582 (2023).
- [10] D. Cogan, Z.-E. Su, O. Kenneth, and D. Gershoni, Deterministic generation of indistinguishable photons in a cluster state, *Nature Photonics* **17**, 324 (2023).
- [11] Y. Meng, C. F. Faurby, M. L. Chan, P. I. Sund, Z. Liu, Y. Wang, N. Bart, A. D. Wieck, A. Ludwig, L. Midolo, *et al.*, Photonic fusion of entangled resource states from a quantum emitter, *arXiv preprint arXiv:2312.09070* (2023).
- [12] Z.-E. Su, B. Taitler, I. Schwartz, D. Cogan, I. Nassar, O. Kenneth, N. H. Lindner, and D. Gershoni, Continuous and deterministic all-photonic cluster state of indistinguishable photons, *Reports on Progress in Physics* **87**, 077601 (2024).
- [13] N. Maring, A. Fyrrillas, M. Pont, E. Ivanov, P. Stepanov, N. Margaria, W. Hease, A. Pishchagin, A. Lemaître, I. Sagnes, *et al.*, A versatile single-photon-based quantum computing platform, *Nature Photonics* **18**, 603 (2024).
- [14] B. B. Blinov, D. L. Moehring, L.-M. Duan, and C. Monroe, Observation of entanglement between a single trapped atom and a single photon, *Nature* **428**, 153 (2004).
- [15] P. Thomas, L. Ruscio, O. Morin, and G. Rempe, Efficient generation of entangled multiphoton graph states from a single atom, *Nature* **608**, 677 (2022).
- [16] J. O’Sullivan, K. Reuer, A. Grigorev, X. Dai, A. Hernández-Antón, M. H. Muñoz-Arias, C. Hellings, A. Flasby, D. C. Zanuz, J.-C. Besse, A. Blais, D. Malz, C. Eichler, and A. Wallraff, Deterministic generation of a 20-qubit two-dimensional photonic cluster state, *arXiv preprint arXiv:2409.06623* (2024).
- [17] A. G. Fowler, A. M. Stephens, and P. Groszkowski, High-threshold universal quantum computation on the surface code, *Phys. Rev. A* **80**, 052312 (2009).
- [18] R. Acharya, L. Aghababaie-Beni, I. Aleiner, T. I. Andersen, M. Ansmann, F. Arute, K. Arya, A. Asfaw, N. Astrakhantsev, J. Atalaya, *et al.*, Quantum error correction below the surface code threshold, *arXiv preprint arXiv:2408.13687* (2024).

- [19] S. J. Devitt, W. J. Munro, and K. Nemoto, Quantum error correction for beginners, *Reports on Progress in Physics* **76**, 076001 (2013).
- [20] M. S. Alam and E. Rieffel, Dynamical logical qubits in the bacon-shor code, *arXiv preprint arXiv:2403.03291* (2024).
- [21] M. S. Kesselring, J. C. Magdalena de la Fuente, F. Thomsen, J. Eisert, S. D. Bartlett, and B. J. Brown, Anyon condensation and the color code, *PRX Quantum* **5**, 010342 (2024).
- [22] O. Higgott and N. P. Breuckmann, Constructions and performance of hyperbolic and semi-hyperbolic Floquet codes, *arXiv preprint arXiv:2308.03750* (2023).
- [23] A. Fahimniya, H. Dehghani, K. Bharti, S. Mathew, A. J. Kollár, A. V. Gorshkov, and M. J. Gullans, Fault-tolerant hyperbolic Floquet quantum error correcting codes, *arXiv preprint arXiv:2309.10033* (2024).
- [24] A. Townsend-Teague, J. Magdalena de la Fuente, and M. Kesselring, Floquetifying the colour code, *Electronic Proceedings in Theoretical Computer Science* **384**, 265–303 (2023).
- [25] M. Davydova, N. Tantivasadakarn, and S. Balasubramanian, Floquet codes without parent subsystem codes, *PRX Quantum* **4**, 020341 (2023).
- [26] G. Üstün, A. Morello, and S. Devitt, Single-step parity check gate set for quantum error correction, *Quantum Science and Technology* **9**, 035037 (2024).
- [27] S. Paesani and B. J. Brown, High-threshold quantum computing by fusing one-dimensional cluster states, *Phys. Rev. Lett.* **131**, 120603 (2023).
- [28] A. Paetznick, C. Knapp, N. Delfosse, B. Bauer, J. Haah, M. B. Hastings, and M. P. da Silva, Performance of planar Floquet codes with majorana-based qubits, *PRX Quantum* **4**, 010310 (2023).
- [29] C. Gidney, M. Newman, A. Fowler, and M. Broughton, A Fault-Tolerant Honeycomb Memory, *Quantum* **5**, 605 (2021).
- [30] S. Bartolucci, P. Birchall, H. Bombin, H. Cable, C. Dawson, M. Gimeno-Segovia, E. Johnston, K. Kieling, N. Nickerson, M. Pant, *et al.*, Fusion-based quantum computation, *Nature Communications* **14**, 912 (2023).
- [31] S. Bartolucci, P. M. Birchall, M. Gimeno-Segovia, E. Johnston, K. Kieling, M. Pant, T. Rudolph, J. Smith, C. Sparrow, and M. D. Vidrighin, Creation of entangled photonic states using linear optics, *arXiv preprint arXiv:2106.13825* (2021).
- [32] S. Omkar, S.-H. Lee, Y. S. Teo, S.-W. Lee, and H. Jeong, All-photonic architecture for scalable quantum computing with greenberger-horne-zeilinger states, *PRX Quantum* **3**, 030309 (2022).
- [33] H. Bombín, C. Dawson, N. Nickerson, M. Pant, and J. Sullivan, Increasing error tolerance in quantum computers with dynamic bias arrangement, *arXiv preprint arXiv:2303.16122* (2023).
- [34] B. Pankovich, A. Neville, A. Kan, S. Omkar, K. H. Wan, and K. Brádler, Flexible entangled-state generation in linear optics, *Physical Review A* **110**, 032402 (2024).
- [35] B. Pankovich, A. Kan, K. H. Wan, M. Ostmann, A. Neville, S. Omkar, A. Sohbi, and K. Brádler, High-photon-loss threshold quantum computing using ghz-state measurements, *Physical Review Letters* **133**, 050604 (2024).
- [36] M. C. Löbl, S. Paesani, and A. S. Sørensen, Loss-tolerant architecture for quantum computing with quantum emitters, *Quantum* **8**, 1302 (2024).
- [37] Y. L. Lim, A. Beige, and L. C. Kwek, Repeat-until-success linear optics distributed quantum computing, *Phys. Rev. Lett.* **95**, 030505 (2005).
- [38] See Supplemental Material at URL-will-be-inserted-by-publisher.
- [39] J. Haah and M. B. Hastings, Boundaries for the Honeycomb Code, *Quantum* **6**, 693 (2022).
- [40] C. Gidney, M. Newman, and M. McEwen, Benchmarking the Planar Honeycomb Code, *Quantum* **6**, 813 (2022).
- [41] In a honeycomb lattice, a vertex is shared by three faces and an edge is shared by two faces. There are thus 3/2 times more edges than vertices for an infinite honeycomb lattice. The 60% reduction thus corresponds to not allocating spin qubits to the edges in the SPOQC-2 architecture, compared to the SPOQC architecture where we need spin qubits for both edges and vertices.
- [42] I. Moflic and A. Paler, On the constant depth implementation of pauli exponentials, *arXiv preprint arXiv:2408.08265* (2024).
- [43] C. Gidney, A Pair Measurement Surface Code on Pentagons, *Quantum* **7**, 1156 (2023).
- [44] X. Ding, Y.-P. Guo, M.-C. Xu, R.-Z. Liu, G.-Y. Zou, J.-Y. Zhao, Z.-X. Ge, Q.-H. Zhang, H.-L. Liu, L.-J. Wang, M.-C. Chen, H. Wang, Y.-M. He, Y.-H. Huo, C.-Y. Lu, and J.-W. Pan, High-efficiency single-photon source above the loss-tolerant threshold for efficient linear optical quantum computing (2023), *arXiv:2311.08347 [quant-ph]*.
- [45] L. A. Pettersson, A. S. Sørensen, and S. Paesani, Deterministic generation of concatenated graph codes from quantum emitters, *arXiv preprint arXiv:2406.16684* (2024).
- [46] R. Chao, M. E. Beverland, N. Delfosse, and J. Haah, Optimization of the surface code design for Majorana-based qubits, *Quantum* **4**, 352 (2020).
- [47] D. Bluvstein, S. J. Evered, A. A. Geim, S. H. Li, H. Zhou, T. Manovitz, S. Ebadi, M. Cain, M. Kalinowski, D. Hangleiter, *et al.*, Logical quantum processor based on reconfigurable atom arrays, *Nature* **626**, 58 (2024).
- [48] M. Cain, C. Zhao, H. Zhou, N. Meister, J. Ataiades, A. Jaffe, D. Bluvstein, and M. D. Lukin, Correlated decoding of logical algorithms with transversal gates, *arXiv preprint arXiv:2403.03272* (2024).
- [49] H. Bombin, D. Litinski, N. Nickerson, F. Pastawski, and S. Roberts, Unifying flavors of fault tolerance with the ZX calculus, *Quantum* **8**, 1379 (2024).
- [50] L. Grans-Samuelsson, R. V. Mishmash, D. Aasen, C. Knapp, B. Bauer, B. Lackey, M. P. d. Silva, and P. Bonderson, Improved Pairwise Measurement-Based Surface Code, *Quantum* **8**, 1429 (2024).
- [51] M. L. Chan, T. J. Bell, L. A. Pettersson, S. X. Chen, P. Yard, A. S. Sørensen, and S. Paesani, Tailoring fusion-based photonic quantum computing schemes to quantum emitters, *arXiv* (2024).
- [52] P. Hilaire, L. Vidro, H. S. Eisenberg, and S. E. Economou, Near-deterministic hybrid generation of arbitrary photonic graph states using a single quantum emitter and linear optics, *Quantum* **7**, 992 (2023).
- [53] C. Gidney, Data for "A Pair Measurement Surface Code on Pentagons" (2022).

- [54] P. Hilaire, T. Dessertaine, B. Bourdoncle, A. Denys, G. De Glinasty, G. Valenti-Rojas, and S. Mansfield, [Simulation material for the article “Enhanced fault-tolerance in photonic quantum computing: Floquet code outperforms surface code in tailored architecture”](#) (2024).
- [55] C. Gidney, Stim: a fast stabilizer circuit simulator, [Quantum](#) **5**, 497 (2021).
- [56] O. Higgott and C. Gidney, Sparse blossom: correcting a million errors per core second with minimum-weight matching, [arXiv preprint arXiv:2303.15933](#) (2023).
- [57] E. Jones, T. Oliphant, P. Peterson, *et al.*, [SciPy: Open source scientific tools for Python](#) (2001–).

SUPPLEMENTARY MATERIAL

$U(\varphi)$ linear-optical interferometers

The spin-optical architectures considered in our work rely on entangling spin qubits with photonic qubits. Gates are then indirectly applied on the spin qubits by means of operations, including measurements, on the spin-entangled photonic qubits (Figure 1).

In the following, we describe the different possible detection patterns and their subsequent effects on spins a and b , assuming these are initially in the normalized states $|\phi_a\rangle = \alpha|0_s\rangle + \beta|1_s\rangle$ and $|\phi_b\rangle = \gamma|0_s\rangle + \delta|1_s\rangle$. The system thus starts in a product state, $|\phi_a\rangle \otimes |\phi_b\rangle$. After the emission process, one obtains

$$(\alpha|0_s\rangle|0_{ph}\rangle + \beta|1_s\rangle|1_{ph}\rangle)(\gamma|0_s\rangle|0_{ph}\rangle + \delta|1_s\rangle|1_{ph}\rangle).$$

The photonic qubits are encoded in a dual-rail: two optical modes per qubit are used and the logical-zero state corresponds to having a photon in the first mode and no photon in the second mode, while the logical-one state has a photon in the second mode and no photon in the first mode,

$$|0_{ph}\rangle = |\overline{10}\rangle, \quad |1_{ph}\rangle = |\overline{01}\rangle,$$

where we used a horizontal bar to indicate Fock states in optical modes. In addition we use $|\overline{0}\rangle$ to denote the vacuum state (in all relevant optical modes). For the rest of the computation, it will be useful to introduce the creation operators, \hat{a}_k^\dagger for $k \in \{0, 1, 2, 3\}$, of each mode k . Note that the two modes of the dual-rail qubit emitted by the first (respectively second) spin will correspond to modes 0 and 1 (respectively modes 2 and 3) of the interferometer. The effect of \hat{a}_k^\dagger on the vacuum state $|\overline{0}\rangle$ is to create a photon in mode k . The state of the system after the emission process can thus be rewritten as

$$(\alpha|0_s\rangle\hat{a}_0^\dagger + \beta|1_s\rangle\hat{a}_1^\dagger)(\gamma|0_s\rangle\hat{a}_2^\dagger + \delta|1_s\rangle\hat{a}_3^\dagger)|\overline{0}\rangle.$$

The optical modes then enter the interferometer. It will be convenient to describe the latter through a matrix,

$$U(\varphi) = \frac{1}{2} \begin{pmatrix} 1 & 1 & 1 & -1 \\ 1 & 1 & -1 & 1 \\ e^{i\varphi} & -e^{i\varphi} & 1 & 1 \\ -e^{i\varphi} & e^{i\varphi} & 1 & 1 \end{pmatrix},$$

indicating how it transforms the creation operators of the four input modes. The choice of the phase φ allows to interpolate between two variants of the architecture. After going through the interferometer, the system is in the state

$$|s_{out}\rangle = (\alpha|0_s\rangle\hat{a}_{0,out}^\dagger + \beta|1_s\rangle\hat{a}_{1,out}^\dagger)(\gamma|0_s\rangle\hat{a}_{2,out}^\dagger + \delta|1_s\rangle\hat{a}_{3,out}^\dagger)|\overline{0}\rangle,$$

where

$$\begin{aligned} \hat{a}_{0,out}^\dagger &= (\hat{a}_0^\dagger + \hat{a}_1^\dagger + e^{i\varphi}\hat{a}_2^\dagger - e^{i\varphi}\hat{a}_3^\dagger)/2, \\ \hat{a}_{1,out}^\dagger &= (\hat{a}_0^\dagger + \hat{a}_1^\dagger - e^{i\varphi}\hat{a}_2^\dagger + e^{i\varphi}\hat{a}_3^\dagger)/2, \\ \hat{a}_{2,out}^\dagger &= (\hat{a}_0^\dagger - \hat{a}_1^\dagger + \hat{a}_2^\dagger + \hat{a}_3^\dagger)/2, \end{aligned}$$

$$\hat{a}_{3,\text{out}}^\dagger = (\hat{a}_0^\dagger + \hat{a}_1^\dagger + \hat{a}_2^\dagger + \hat{a}_3^\dagger)/2.$$

Depending on the detection patterns of the photons, the spin qubits are projected onto different states. To synthesize the outcomes, for each detection pattern, we list the amplitude of every spin-qubit state in the canonical basis (Table S1). Thus, the outcome spin-qubit state $|s_{\text{out}}\rangle$ of every detection pattern can be read on the table's rows.

	$\alpha\gamma 0_s\rangle 0_s\rangle$	$\alpha\delta 0_s\rangle 1_s\rangle$	$\beta\gamma 1_s\rangle 0_s\rangle$	$\beta\delta 1_s\rangle 1_s\rangle$
$\hat{a}_0^\dagger\hat{a}_0^\dagger$	1	-1	1	-1
$\hat{a}_1^\dagger\hat{a}_1^\dagger$	-1	1	-1	1
$\hat{a}_2^\dagger\hat{a}_2^\dagger$	$e^{i\varphi}$	$e^{i\varphi}$	$-e^{i\varphi}$	$-e^{i\varphi}$
$\hat{a}_3^\dagger\hat{a}_3^\dagger$	$-e^{i\varphi}$	$-e^{i\varphi}$	$e^{i\varphi}$	$e^{i\varphi}$
$\hat{a}_0^\dagger\hat{a}_1^\dagger$	0	0	0	0
$\hat{a}_2^\dagger\hat{a}_3^\dagger$	0	0	0	0
$\hat{a}_0^\dagger\hat{a}_2^\dagger$	$1 + e^{i\varphi}$	$1 - e^{i\varphi}$	$1 - e^{i\varphi}$	$1 + e^{i\varphi}$
$\hat{a}_0^\dagger\hat{a}_3^\dagger$	$1 - e^{i\varphi}$	$1 + e^{i\varphi}$	$1 + e^{i\varphi}$	$1 - e^{i\varphi}$
$\hat{a}_1^\dagger\hat{a}_2^\dagger$	$1 - e^{i\varphi}$	$1 + e^{i\varphi}$	$1 + e^{i\varphi}$	$1 - e^{i\varphi}$
$\hat{a}_1^\dagger\hat{a}_3^\dagger$	$1 + e^{i\varphi}$	$1 - e^{i\varphi}$	$1 - e^{i\varphi}$	$1 + e^{i\varphi}$

Table S1: Table representation of the state $|s_{\text{out}}\rangle$, up to normalization, separating photonic creation operators, acting on the vacuum state $|\bar{0}\rangle$ (rows) and spin-qubit states (columns)

Repeat-type patterns

When photons bunch into a single output mode, single-qubit operations are applied on the spins. These operations can easily be corrected such that the interferometer effectively applies an identity gate in these cases. Looking at the first row of Table S1, we see that if two photons are detected in mode 0, then the spin states are

$$\alpha\gamma|0_s\rangle|0_s\rangle - \alpha\delta|0_s\rangle|1_s\rangle + \beta\gamma|1_s\rangle|0_s\rangle - \beta\delta|1_s\rangle|1_s\rangle,$$

which is equal to $Z_b|\phi_a\rangle|\phi_b\rangle$. Measuring the two photons in mode 0 thus effectively applies a Z operation on the second spin qubit. Likewise, looking at the subsequent three rows of Table S1, it is not hard to find the different two-spin states (up to global phase factors) associated with bunching detection patterns,

$$\left. \begin{array}{l} (0,0) \\ (1,1) \end{array} \right\} \longrightarrow Z_b|\phi_a\rangle|\phi_b\rangle,$$

$$\left. \begin{array}{l} (2,2) \\ (3,3) \end{array} \right\} \longrightarrow Z_a|\phi_a\rangle|\phi_b\rangle.$$

In both cases, applying a Z operation on one of the qubits recovers the identity gate.

Success-type patterns

When photons are detected in different modes, a non-trivial two-qubit gate is applied on both spins. Denoting by $|\Phi_{ab}^+\rangle = \alpha\gamma|0_s\rangle|0_s\rangle + \beta\delta|1_s\rangle|1_s\rangle$ and $|\Psi_{ab}^+\rangle = \alpha\delta|0_s\rangle|1_s\rangle + \beta\gamma|1_s\rangle|0_s\rangle$, we have the spin states (up to normalization and global phase factors) for successful detection patterns

$$\left. \begin{array}{l} (0,2) \\ (1,3) \end{array} \right\} \longrightarrow \cos \frac{\varphi}{2} |\Phi_{ab}^+\rangle + i \sin \frac{\varphi}{2} |\Psi_{ab}^+\rangle,$$

$$\left. \begin{matrix} (0, 3) \\ (1, 2) \end{matrix} \right\} \longrightarrow i \sin \frac{\varphi}{2} |\Phi_{ab}^+\rangle + \cos \frac{\varphi}{2} |\Psi_{ab}^+\rangle.$$

In contrast with the repeat-type detection patterns, the phase parameter φ determines the specific two-qubit operation applied. In the following, we focus on two cases $\varphi = 0$ and $\varphi = \pi/2$.

$\varphi = 0$ In this case, the interferometer performs a non-destructive ZZ measurement: if we detect photons in modes (0, 2) and (1, 3) (resp. (0, 3) and (1, 2)) spins are in the state $|\Phi_{ab}^+\rangle$ (resp. $|\Psi_{ab}^+\rangle$) corresponding to a +1 (resp. -1) ZZ-measurement outcome.

$\varphi = \pi/2$ Here, we need to apply single-qubit corrections to retrieve a CZ gate. Indeed, up to normalization, we get the two-spin states

$$\left. \begin{matrix} (0, 2) \\ (1, 3) \end{matrix} \right\} \longrightarrow |\Phi_{ab}^+\rangle + i |\Psi_{ab}^+\rangle,$$

$$\left. \begin{matrix} (0, 3) \\ (1, 2) \end{matrix} \right\} \longrightarrow i |\Phi_{ab}^+\rangle + |\Psi_{ab}^+\rangle.$$

Applying $S_a^\dagger S_b^\dagger$ to the first two cases and $S_a S_b$ to the last two, where $S = \sqrt{Z}$ is the phase gate, we have

$$\left. \begin{matrix} (0, 2) \\ (1, 3) \end{matrix} \right\} \longrightarrow \alpha\gamma |0_s\rangle |0_s\rangle + \alpha\delta |0_s\rangle |1_s\rangle + \beta\gamma |1_s\rangle |0_s\rangle - \beta\delta |1_s\rangle |1_s\rangle,$$

$$\left. \begin{matrix} (0, 3) \\ (1, 2) \end{matrix} \right\} \longrightarrow i(\alpha\gamma |0_s\rangle |0_s\rangle + \alpha\delta |0_s\rangle |1_s\rangle + \beta\gamma |1_s\rangle |0_s\rangle - \beta\delta |1_s\rangle |1_s\rangle),$$

which corresponds to a CZ gate applied on the two spins, up to a global phase factor.

Error models

Here, we present the error models that we used in the simulations. Importantly, the errors are the same for both the RUS CZ and for the RUS M_{ZZ}, allowing to compare them easily. We consider spin decoherence, photon distinguishability, and photon loss as the relevant sources of errors. The error model corresponding to photon loss is discussed in the main text.

Spin coherence time For the simulations, we consider that the timescale t_{RUS} of a RUS operation is much larger than the rest of the single-qubit operations (initializations, gates, and measurements). This is motivated by the fact that this gate requires a feed-forward operation. The main error mechanism affecting the quantum information storage of spin qubits is decoherence [6], characterized by the spin coherence time T_2 is assumed to be much smaller than the spin relaxation time T_1 , $T_2 \ll T_1$. Under this assumption, the error channel corresponding to spin decoherence is:

$$\mathcal{C}_{\text{dec}}(\rho) = (1 - p_Z)\rho + p_Z Z\rho Z,$$

with

$$p_Z = \frac{1}{2} \left(1 - \exp \left[-\frac{t_{\text{RUS}}}{T_2} \right] \right).$$

Note that the larger the ratio t_{RUS}/T_2 is, the more decoherence occurs. We refer the reader to Appendix C of Ref. [6] for the full derivation. We will assume that spin decoherence independently acts on all qubits during the implementation of the RUS operations.

Distinguishability We also use the error model from Ref. [6] to simulate the distinguishability error between two photons originating from different sources. Whenever a RUS operation is applied to spin qubits a and b , we apply the (unheralded) error channel

$$\mathcal{C}_D(\rho) = (1 - D)\rho + D\mathcal{C}_a \circ \mathcal{C}_b(\rho)$$

with \mathcal{C}_i defined as in the main text and D the photon distinguishability.

Generalization for M_{XX} and M_{YY} operations

To implement the measurement sequences of a honeycomb code, in addition to M_{ZZ} , we need to perform M_{XX} and M_{YY} measurements. As shown in Figures S1-(a), S1-(b), M_{XX} and M_{YY} measurements are obtained by the conjugation of M_{ZZ} with, respectively, H or H_{YZ} gates. A Hadamard gate $H = (X + Z)/\sqrt{2}$ (respectively $H_{YZ} = (Y + Z)/\sqrt{2}$) gate converts a Z error into an X (Y) error. It is thus easy to keep track of errors for these measurements as well. For example, since photon loss in RUS M_{ZZ} leads to a double phase erasure, i.e. a double Z erasure, photon loss in the implementation of an M_{XX} gate will lead to a double X (bit) erasure of the spin qubits, with the same probability p_{RUS} . Likewise, in an M_{YY} -measurement it yields a double Y erasure. Similarly, we can convert the Z error channel induced by the spin decoherence and the photon distinguishability into X or Y error channels for the RUS M_{XX} and the M_{YY} operations.

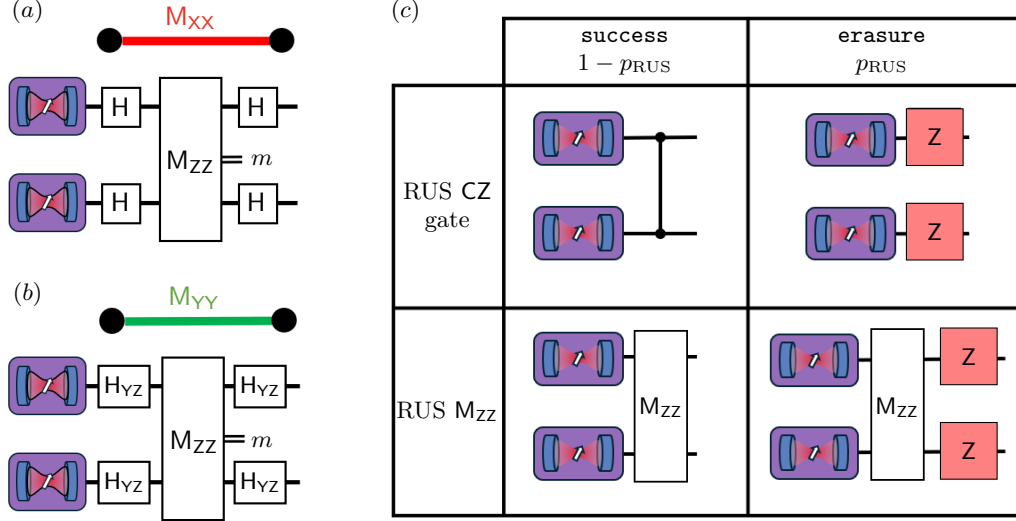


Figure S1: Implementation of (a) M_{XX} and (b) M_{YY} gates for the SPOQC-2 architecture. (c) Circuits corresponding to the different outcomes of the RUS operations. In the **erasure** case, red Z boxes correspond to applying the identity or the Z gate with probability $1/2$, which corresponds to the error channel \mathcal{C}_i from the main text.

Simulation methods

Circuit building

For the simulations, we used the “.stim” circuits made available in Ref. [53] for the work in Ref. [43]. In these circuits, we removed the error model that was previously introduced as well as Stim’s REPEAT blocks. On these noiseless circuits, we have added our own noise model described in the previous sections. For more information, see our publicly available code [54].

Circuit sampling

Whether we consider the standard SPOQC architecture or its two-qubit-measurement variant, SPOQC-2, we can group errors into two categories: heralded errors which are the erasures coming from photon loss, and unheralded errors, comprising photon distinguishability and spin decoherence. Unheralded errors can be treated in a standard way using Stim’s stabilizer simulator [55], as long as the error channel describing the process is a Pauli channel.

In the current framework, heralded errors are caused by photon loss when implementing the RUS operations between spin qubits using RUS linear-optical gates. As explained in the main text, one of three events can happen when detecting the output of the RUS gates:

1. two photons are detected in a **repeat** measurement pattern such that the identity gate is applied on both spins and the gate is repeated,
2. two photons are detected in a **success** measurement pattern such that the desired operation is effectively applied on both spins and the gate succeeds,
3. less than two photons are detected which leads to an **erasure** detection pattern and a complete phase erasure for both spins. If one allows for infinitely many trials, the RUS gate has a failure probability of

$$p_{\text{RUS}} = p_e \sum_{n=0}^{\infty} (p_r)^n = \frac{p_e}{1 - p_r} = \frac{2 - 2(1 - \varepsilon)^2}{2 - (1 - \varepsilon)^2},$$

that depends on the single-photon loss rate ε and where $p_e = 1 - (1 - \varepsilon)^2$, $p_r = (1 - \varepsilon)^2/2$ are the **erasure** and **repeat** probabilities defined in the main text.

Since this error depends on the measurement pattern at the output of the gate, each time we read out the trial outcome we know whether an error channel has been applied; this is an erasure.

Simulation for erasure errors

In order to simulate erasures using Stim's stabilizer simulator [55], we go through a *pre-processing step* that will build instances of QEC circuits with known heralded error channels. Let us consider a QEC circuit with \mathcal{N}_{RUS} gates. Whether these gates implement spins CZ gates or \mathbf{M}_{ZZ} does not matter. For each RUS gate, we implicitly allow for an infinite number of **repeat** outcomes to happen. Consequently, the RUS operations can be described with a simple coin toss leading to an **erasure** outcome with probability $1 - p_{\text{RUS}}$. In that case, a phase erasure on each spin is applied. The RUS CZ gate acts on the phase of the two spin qubits, so there is no point in proceeding to another trial after the phases have been erased. On the other hand, an \mathbf{M}_{ZZ} -measurement commutes with phase erasures and we can still retrieve the measurement outcome by repeating the RUS procedure until we reach a successful outcome. If we carry out this process for each of the \mathcal{N}_{RUS} RUS gates in the circuit, we build a random instance of the QEC circuit with known error channels that can be simulated using Stim's stabilizer simulator. As an illustration, Figure S1-(c) gives an example of the process for a simple circuit.

For each circuit \mathcal{C} that we build using the method just described, we estimate the corresponding logical error rate $\varepsilon_L(\mathcal{C})$ using Stim's stabilizer simulator. Instances of the stabilizer measurements (or check measurements for Floquet codes) are randomly sampled and fed to a Minimum Weight Perfect Matching decoder implemented in the Pymatching library [56]. For the i -th instance, we compare the outcome D_i guessed by the decoder to the logical measurement L_i provided by a data readout at the end of the circuit: whenever these are different, it means a logical error occurred. We observe empirically that circuit instances \mathcal{C} belong to one of two categories:

- (a) circuits where the decoder is always able to recover the logical information, in which case $\varepsilon_L(\mathcal{C}) = 0$, or
- (b) circuits where the decoder randomly guesses the logical state, and $\varepsilon_L(\mathcal{C}) = 1/2$.

For erasure errors, even if too slow, Gaussian elimination is a valid decoding scheme. Circuit classification into categories (a) and (b) can be seen as a successful Gaussian elimination, in which case physical errors are identified and logical information can be recovered, or unsuccessful Gaussian elimination, where the decoder could not identify physical errors and gives a random prediction for the logical information. We use this knowledge to build the following estimator $\hat{\varepsilon}_L(\mathcal{C})$ for the instance-specific logical error rate,

$$\hat{\varepsilon}_L(\mathcal{C}) = \begin{cases} 0 & \text{if } \forall i \in \{1, \dots, N\}, D_i = L_i \\ \frac{1}{2} & \text{otherwise,} \end{cases} \quad (\text{S1})$$

where N is the number of instances generated. If a circuit belongs to the first category, no mismatch can ever be seen so the circuit will never be misclassified. On the other hand, a circuit of the second type, has an exponentially small probability $(1/2)^N$ to be put in the wrong category since we are limited by the number N of instances (D_i, L_i) generated. For the chosen value of $N = 256$ in our simulations, this probability is negligible though, so we assume that such events do not occur.

The overall logical error rate ε_L is finally obtained by computing the weighed average of the individual logical error rates of all possible circuits

$$\varepsilon_L = \sum_{\mathcal{C}} \varepsilon_L(\mathcal{C}) p_{\mathcal{C}},$$

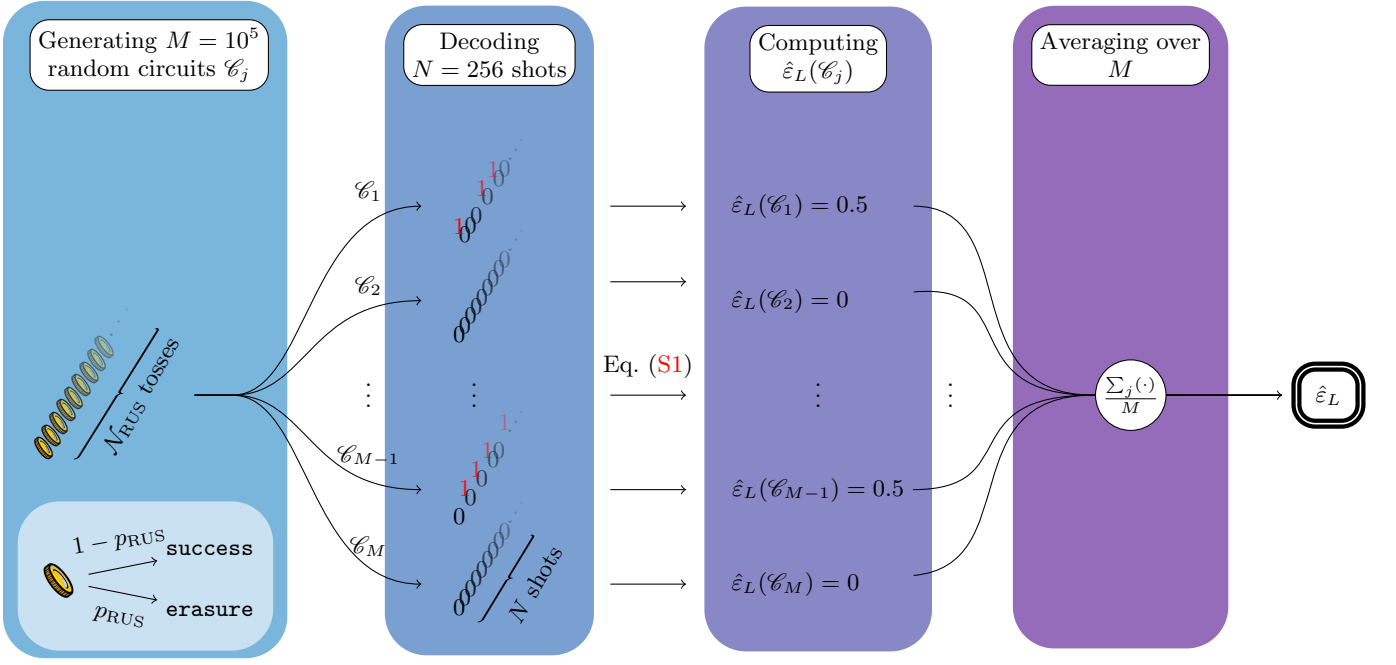


Figure S2: Simulation pipeline from left to right for **erasure** errors. We start by simulating \mathcal{N}_{RUS} coin tosses with outcomes **success** with probability $1 - p_{\text{RUS}}$ and **erasure** with probability p_{RUS} . To each coin we associate a RUS gate whose status after the toss is determined by Figure S1(c). We carry out this process $M = 10^5$ times and generate M instances $(\mathcal{C}_j)_{j=1,\dots,M}$ of the QEC circuit. We sample each circuit $N = 256$ times. For each sample i , we compare the decoder outcome D_i and the logical information readout. Anytime there is a mismatch, we record a logical error represented by red 1s in the figure. Following Eq. (S1), we classify circuit instances into one of two categories: $\hat{\varepsilon}_L(\mathcal{C}) = 0$ or $\hat{\varepsilon}_L(\mathcal{C}) = 0.5$. We finally average over the M classification outcomes to obtain our estimator $\hat{\varepsilon}_L$ for the logical error rate.

where $p_{\mathcal{C}}$ is the probability to obtain circuit \mathcal{C} . As RUS gates are independent in the circuit, we can re-express this average as

$$\varepsilon_L = \sum_{k=0}^{\mathcal{N}_{\text{RUS}}} \binom{\mathcal{N}_{\text{RUS}}}{k} p_{\text{RUS}}^k (1 - p_{\text{RUS}})^{\mathcal{N}_{\text{RUS}} - k} \sum_{\mathcal{C} \in \mathbf{C}_k} \varepsilon_L(\mathcal{C}),$$

where \mathbf{C}_k is the set of circuits with exactly k failed RUS gates. As the number of RUS gates rapidly increases with the size of the QEC code considered, it quickly becomes unfeasible to simulate the $2^{\mathcal{N}_{\text{RUS}}}$ possible circuits. We therefore build an estimator $\hat{\varepsilon}_L$ of the logical error rate by averaging the estimators $\hat{\varepsilon}_L(\mathcal{C})$ computed for $M = 10^5$ random instances of circuits $\mathcal{C}_{j=1,\dots,M}$ generated by the process previously described,

$$\hat{\varepsilon}_L = \frac{1}{M} \sum_{j=1}^M \hat{\varepsilon}_L(\mathcal{C}_j). \quad (\text{S2})$$

Figure S2 offers a summary of the simulation process for **erasure** errors.

Simulation for distinguishability and decoherence errors

As distinguishability and decoherence are described by Z error channels, we can directly rely on Stim to estimate the logical error rate. We sample our circuits $N = 10^5$ times and compare the decoder outcome D_i and the logical measurement L_i for sample i . The estimator for the logical error rate is therefore

$$\hat{\varepsilon}_L = 1 - \frac{1}{N} \sum_{i=1}^N \delta_{D_i, L_i}. \quad (\text{S3})$$

Simulation results

Confidence intervals for erasure simulations

To obtain confidence intervals for ε_L in the case of erasure errors, we compute the unbiased sample variance \hat{S}_L^2 defined by

$$\hat{S}_L^2 = \frac{1}{M-1} \sum_{j=1}^M (\hat{\varepsilon}_L(\mathcal{C}_j) - \hat{\varepsilon}_L)^2.$$

Since $2\hat{\varepsilon}_L(\mathcal{C}_j) \in \{0, 1\}$ and therefore $(2\hat{\varepsilon}_L(\mathcal{C}_j))^2 = 2\hat{\varepsilon}_L(\mathcal{C}_j)$, we can easily show that

$$\hat{S}_L^2 = \frac{M}{M-1} \hat{\varepsilon}_L \left(\frac{1}{2} - \hat{\varepsilon}_L \right). \quad (\text{S4})$$

As the samples $\hat{\varepsilon}_L(\mathcal{C}_j)$ are independent and identically distributed random variables, the confidence interval is given by

$$\text{CI}_\alpha = \left[\hat{\varepsilon}_L - \mathbf{t}_{\alpha, M-1} \frac{\hat{S}_L}{\sqrt{M}}, \hat{\varepsilon}_L + \mathbf{t}_{\alpha, M-1} \frac{\hat{S}_L}{\sqrt{M}} \right],$$

with α the confidence level, and $\mathbf{t}_{\alpha, M-1}$ the scaling factor given by Student's t -distribution. In our simulations, we use $\mathbf{t}_{0.999, \infty} = 3.291$.

Confidence intervals for distinguishability and decoherence simulations

As in the erasure case, the unbiased sample variance can be obtained easily and reads

$$\hat{S}_L^2 = \frac{N}{N-1} \hat{\varepsilon}_L (1 - \hat{\varepsilon}_L), \quad (\text{S5})$$

where we used $(1 - \delta_{D_i, L_i})^2 = 1 - \delta_{D_i, L_i}$. The confidence interval is obtained in the same way as the erasure case.

Threshold derivation (Table I)

Here, we present the different figures, from which we derived the fault-tolerant threshold for each individual native operation CZ or M_{ZZ}, each code HC or SC, and each individual noise mechanism.

For each code family (HC or SC) parameterized by its distance d , the threshold for an error parameter p can be visualized as the crossing point between the curves $p \mapsto \varepsilon_L(p, d)$ as $d \rightarrow \infty$. In our case, since we cannot simulate codes of infinitely large distances nor have exact analytical formulas, we approximate thresholds using the following steps:

- (i) We choose a vector of evenly-spaced error parameters $(p_i)_{i=1, \dots, k}$ (with $p_i < p_{i+1}$).
- (ii) For each p_i , we compute the estimator of the logical error rate $\hat{\varepsilon}_L(p_i, d)$ at a given code distance d , using the methods described in previous sections.
- (iii) We fit the empirical noisy data $(p_i, \hat{\varepsilon}_L(p_i, d_j))_{i=1, \dots, k}$ with a polynomial of order 4 using Scipy's `scipy.curve_fit` routine [57]. The latter returns polynomial coefficients $(\hat{a}_j(d))_{j=0, \dots, 4}$ along with a covariance matrix $C(d)$ with coefficients $ij \text{ Cov}(\hat{a}_i(d), \hat{a}_j(d))$ measuring the noise-induced uncertainty of the polynomial coefficients. The degree of the polynomial was chosen heuristically to be $n = 4$ as it achieves a reasonably good fit (with around unit standardized χ^2). Other values of n were tested but did not significantly change the results.
- (iv) For distances d_{\max} and $d_{\max} - 2$ (where d_{\max} is the largest distance simulated), we randomly draw the polynomial coefficients of $K = 10^4$ pairs of polynomials, $Q_{d_{\max}}$ and $Q_{d_{\max} - 2}$, according to a multivariate normal law with mean vector $(\hat{a}_j(d))_{j=0, \dots, 4}$ and covariance matrix $C(d)$.
- (v) For each pair, we find the intersection point \hat{p}_{int} between the curves $p \mapsto Q_{d_{\max}}(p)$ and $p \mapsto Q_{d_{\max} - 2}(p)$. We keep the results for which there is a single intersection in the range $[p_1, p_k]$.

(vi) We finally compute an estimator of the threshold for error parameter p as

$$\hat{p}_{th} = \frac{1}{K} \sum_{k=1}^K \hat{p}_{int,k},$$

along with its sample variance

$$\hat{S}_{th}^2 = \frac{1}{K-1} \sum_{k=1}^K (\hat{p}_{int,k} - \hat{p}_{th})^2.$$

These steps ensure that both the uncertainty on the data and the fit are taken into account to estimate threshold values. The estimated value is displayed on Figure 3 of the main text for erasure errors, as well as on Figure S3 for all types of errors, as a gray dotted line. The shaded gray regions correspond to a two-sided one-standard deviation interval around \hat{p}_{th} .

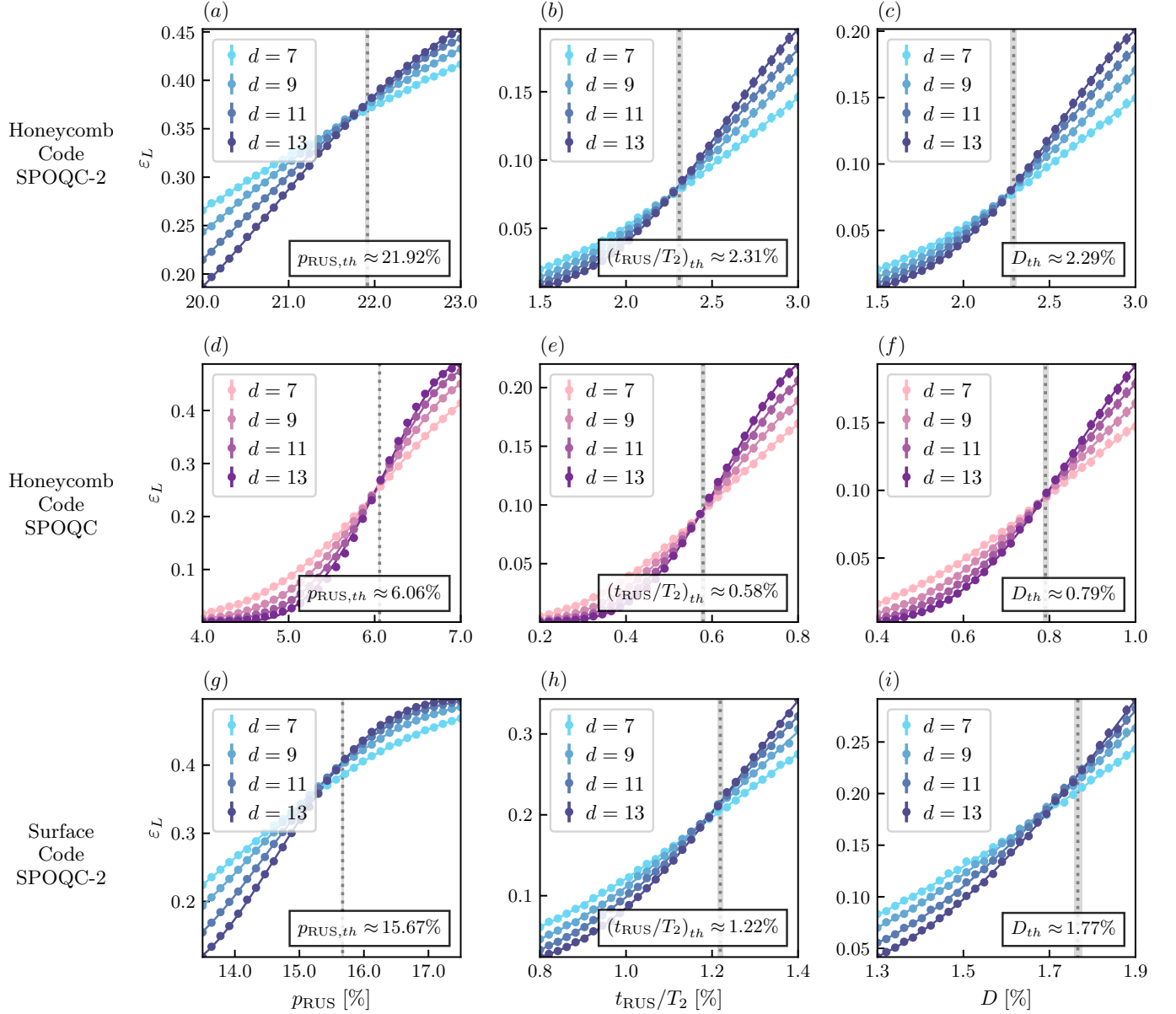


Figure S3: Logical error rates as a function of RUS failure probability p_{RUS} , decoherence fraction t_{RUS}/T_2 and photon distinguishability D for the Honeycomb Code and the Surface Code in the SPOQC and SPOQC-2 architectures. These estimation are obtained according to the protocol described in section "Threshold derivation (Table I)" for $K = 10^4$. For erasure errors, we classified $M = 10^5$ circuits on $N = 256$ samples. For decoherence and dinstiguishability errors, we used $N = 10^5$ samples to estimate the logical error rate. Error bars represent 99.9%-confidence intervals of the data points. The dotted line positions the approximate threshold computed using the method described previously. When represented, gray regions encapsulate parameters p_{RUS} , t_{RUS}/T_2 and D lying in one-standard-deviation intervals around the thresholds. We chose not to represent them whenever the interval is too narrow. We obtain the thresholds (a) $p_{\text{RUS},th} = 21.92\% \pm 0.02\%$, (b) $(t_{\text{RUS}}/T_2)_{th} = 2.309\% \pm 0.018$, (c) $D_{th} = 2.292\% \pm 0.018\%$, (d) $p_{\text{RUS},th} = 6.057\% \pm 0.009\%$, (e) $(t_{\text{RUS}}/T_2)_{th} = 0.579\% \pm 0.006$, (f) $D_{th} = 0.791\% \pm 0.007\%$, (g) $p_{\text{RUS},th} = 15.67\% \pm 0.017\%$, (h) $(t_{\text{RUS}}/T_2)_{th} = 1.219\% \pm 0.007\%$, (i) $D_{th} = 1.766\% \pm 0.009\%$.